A hybrid model of laser energy deposition for multi-dimensional simulations of plasmas and metals

Mikhail M. Basko, Ilia P. Tsygvintsev

Keldysh Institute of Applied Mathematics RAS, Miusskaya sq., 4, Moscow, 125047, Russia

RnD-ISAN/EUV Labs, Promyshlennaya Str., 1A, Moscow-Troitsk, 142191, Russia

Abstract

The hybrid model of laser energy deposition is a combination of the geometrical-optics ray-tracing method with the one-dimensional (1D) solution of the Helmholtz wave equation in regions where the geometrical optics becomes inapplicable. We propose an improved version of this model, where a new physically consistent criterion for transition to the 1D wave optics is derived, and a special rescaling procedure of the wave-optics deposition profile is introduced. The model is intended for applications in large-scale two- and three-dimensional hydrodynamic codes. Comparison with exact 1D solutions demonstrates that it can fairly accurately reproduce the absorption fraction in both the *s*- and *p*-polarizations on arbitrarily steep density gradients, provided that a sufficiently accurate algorithm for gradient evaluation is used. The accuracy of the model becomes questionable for long laser pulses simulated on too fine grids, where the hydrodynamic self-focusing instability strongly manifests itself.

Keywords: Laser absorption, laser plasmas, ray tracing
PACS: 52.25.Os, 52.38.Dx, 52.38.Mf, 02.60.Lj
Published: Computer Physics Communications, vol. 214, pp.59-70 (2017); DOI: 10.1016/j.cpc.2017.01.010

1. Introduction

An important ingredient in any large-scale hydrodynamic code, aimed at simulations of laser plasmas, must be a model for propagation and absorption of laser light in dynamic and non-uniform plasmas. The most widely used approach is based on tracing individual elementary laser rays in the geometrical optics (GO) approximation [1], which is based on the assumptions that the characteristic spatial scale of plasma parameter variation $L \gg \lambda$, and that the attenuation of the laser light over a distance of one wavelength λ is weak — i.e. that $\kappa'' \ll 1$, where $\kappa'' = \Im(\sqrt{\varepsilon})$ is the imaginary part of the refractive index, ε is the dielectric permittivity. The ray-tracing (RT) method has apparent advantages of a relative simplicity by implementation, of comparatively low computing costs in two (2D) and three (3D) dimensions, and of the ability to describe refraction. However, its applicability conditions are certainly violated in the vicinity of the critical surface, defined by the condition

$$n_e = n_{cr} \equiv \frac{m_e\omega^2}{4\pi e^2}, \tag{1}$$

where n_e is the number density of free electrons, $\omega = 2\pi c/\lambda$ is the angular frequency of the laser light, m_e and $-e$ are, respectively, the electron mass and charge, c is the speed of light. Therefore, beside inability to reproduce diffraction, the RT approach cannot provide adequate description of such important physical effects as (i) reflection, transmission and absorption of laser light by metallic films and overdense plasma layers, and (ii) distinction between the *s*- and *p*-polarizations (including the resonant absorption of the latter) by oblique incidence onto rising profiles of n_e.

Within the framework of linear optics, a cardinal improvement versus the GO-based RT method would be a direct solution of the Helmholtz wave equation [2], and it has been successfully used in one-dimensional (1D) laser-plasma simulations [3, 4]. But implementation of this method in large-scale 2D and 3D codes meets severe challenges, although attempts in this direction have been undertaken [5]. The most acute problem is the ne-

Email address: mmbasko@gmail.com (Mikhail M. Basko)
URL: www.basko.net (Mikhail M. Basko)

cessity to resolve very small spatial scales, down to a fraction of the skin depth, which in dense plasmas and typical metals may be as small as $\delta = (2\kappa''\omega/c)^{-1} \simeq 20$–40 nm. Clearly, numerical simulations of most practically important laser-plasma problems cannot be conducted in 2D and 3D with a mesh resolution of a few nanometers.

In 1D this problem is usually circumvented by applying a finite analytic numerical method [6, 7] to solve the corresponding 1D Helmholtz equation, as is, for example, described in detail in Ref. [4] and in Section 2.2 below. In contrast to conventional finite difference schemes, where the derivatives are replaced by finite differences, a finite analytic method relies on the exact analytic solutions of the linearized original differential equations across each mesh zone. From the physics point of view, this brings a decisive advantage in situations, where a crude mesh cannot resolve the spatial scale δ over which the light intensity decays — as is typically the case in the evanescence zone below the critical surface in 2D and 3D problems.

The latter point can be illustrated as follows. If we consider a single mesh zone of dimensionless (in units of c/ω) thickness $\bar{h}$, across which the permittivity ε is assumed to be constant, the exact solution of the Helmholtz equation (6) in the evanescence zone will be $|E_h/E_0| = \exp(-\kappa''\bar{h})$, which is exactly reproduced by the finite analytic method. At the same time, if we apply the lowest-order implicit (only implicit methods can treat "optically thick" cells with $\kappa''\bar{h} > 1$) finite difference scheme, we obtain $|E_h/E_0| = (1+\kappa''\bar{h})^{-1}$ — which may deviate from the physically correct answer by several orders of magnitude when $\kappa''\bar{h} \gg 1$.

The above argument leads to a conclusion that a full-scale implementation of the 2D (3D) Helmholtz wave equation into a large-scale hydrodynamic code does not look as an appealing option unless it is based on an appropriate 2D (3D) finite analytic numerical algorithm. However, to the best of our knowledge, such algorithms still have not been developed.

Here we advocate a simpler approach, namely, a hybrid model of laser deposition which combines the RT algorithm in a low density region with a solution of the 1D wave-equation near the critical surface. This model has already been employed in one or another form by several authors [8, 9]. In this work we make a next step in its development, namely, we formulate a new criterion for transition from the geometrical to wave optics, based on a consistent derivation from the condition of applicability of the geometrical optics. Also, we propose a special rescaling procedure for the 1D wave-optics deposition profile, which ensures smooth matching in space between the GO- and WO-generated deposition powers — independent of the values of the free parameters in the transition criterion. The conducted numerical tests against known exact solutions confirm that our modifications significantly improve the accuracy and robustness of the hybrid model in describing laser absorption in non-uniform plasmas.

It should be emphasized that the present theoretical description remains entirely within the framework of linear optics, where the optical properties of the medium are assumed to be fully represented by its complex dielectric permittivity ε, which does not depend on the laser intensity. As in the traditional RT method, the effects of diffraction are completely ignored. A possible way to overcoming the latter shortcoming was recently proposed in Refs. [10, 11].

The outline of the paper is as follows. In Section 2 we give mathematical description of the modifications to the hybrid model, proposed in this work. Section 3 briefly outlines specifics of its implementation into the 2D radiation-hydrodynamics code RALEF, used to run the numerical tests. In Section 4 the results of tests against exact 1D solutions for a piecewise linear ε profile are presented. Two 2D numerical examples, analyzed in Section 5, illustrate two different physical situations: one, where the present model is expected to produce fairly accurate results for the distribution of the absorbed laser power, and another, where its eclectic character and the absence of diffraction have a pronounced detrimental effect on the ability to adequately describe laser absorption in a plasma.

2. Description of the model

2.1. General outline

Conceptually, the model proposed here is a relatively simple extension of the RT model by Kaiser [1]. We consider propagation of a monochromatic laser light with an angular frequency ω in a medium with a given (for this frequency) complex dielectric permittivity [12]

$$\varepsilon \equiv \varepsilon' + i\varepsilon'' = 1 - \frac{\omega_p^2}{\omega(\omega + i\nu_{ei})}, \qquad (2)$$

where $\omega_p^2 = 4\pi n_e e^2/m_e$ is the square of the plasma frequency, ν_{ei} is the electron-ion collision frequency, and $i = \sqrt{-1}$, ; $\varepsilon = \varepsilon(\mathbf{x})$ is a function of the position $\mathbf{x}$ in space.

As in the traditional RT approach, the incident laser beam is represented by a bundle of a large number of infinitely thin elementary rays, each of which carries a

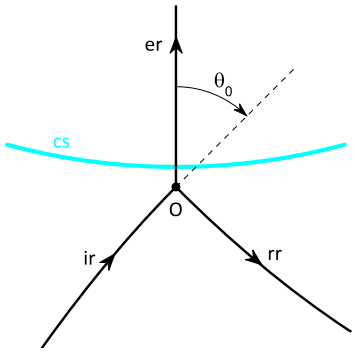

Figure 1: Splitting of the incident geometric ray *ir* at the transition point *O* near the critical surface *cs* into the reflected geometric ray *rr* and the "evanescent" ray *er*. The evanescent ray propagates along the local normal to the critical surface into the overdense plasma.

certain power P_r. In a typical situation, every elementary ray enters the computational domain from an underdense side, where $n_e \ll n_{cr}$ and the approximation of geometrical optics applies. There the GO trajectory $\mathbf{x}_r(\tau)$ of a ray r is calculated by solving the equation [13, 1]

$$\frac{d^2\mathbf{x}_r}{d\tau^2} = \frac{1}{2}\nabla\varepsilon_{cp} = -\frac{1}{2}\nabla\bar{n}_e, \quad \bar{n}_e \equiv \frac{n_e}{n_{cr}}, \tag{3}$$

where τ is a parameter (with the dimension of length) along the ray trajectory ($\tau = ct$ in Ref. [1]). Because the applicability of GO requires $\varepsilon'' \ll |\varepsilon'|$, i.e. $\nu_{ei} \ll \omega$ in Eq. (2), the cold-plasma permittivity

$$\varepsilon_{cp} = 1 - \frac{\omega_p^2}{\omega^2} = 1 - \bar{n}_e \tag{4}$$

is used in Eq. (3) instead of ε' from Eq. (2). The attenuation of the GO ray power $P_r(\tau)$ is calculated in the next approximation with respect to the small parameter ν_{ei}/ω from the equation

$$\frac{dP_r}{d\tau} = -\frac{\omega}{c}\varepsilon''\,P_r. \tag{5}$$

Our principal modification of the classical RT model is in that the trajectory of every incident GO ray is traced up to a certain point O (see Fig. 1) in the vicinity of the critical surface, where the condition for transition to the wave optics (WO) is fulfilled, and where the incident ray power $P_r = P_{ir}$ is split between the reflected (*rr*) and the "evanescent" (*er*) rays. In particular, upon reaching the point O, a 1D Helmholtz equation is solved for the *s*- and *p*-polarized components of a planar wave, incident on an imaginary planar layer lying perpendicular to the gradient of ε_{cp}, i.e. to the vector $\nabla\bar{n}_e$ at O. The variation axis (axis z in Section 2.2 below) across this planar layer is represented by a straight evanescent ray *er*, emerging from point O in the direction of $\nabla\bar{n}_e$. The angle of incidence θ_0 is then the angle between the *ir* and the *er* rays. The required 1D profile of the dielectric permittivity $\varepsilon(z)$ is calculated by tracing the evanescent ray *er* across the main 2D (or 3D) numerical grid.

Solution of this 1D WO problem yields the reflected fractions $f_{rfl}^{(s)}$ and $f_{rfl}^{(p)}$ of the incident power in, respectively, the *s*- and *p*-polarizations. Having split the incident power P_{ir} of the GO ray *ir* at point O into its *s*- and *p*-components, $P_{ir} = P_{ir}^{(s)} + P_{ir}^{(p)}$, one readily obtains the *s*- and *p*-components, $P_{rr}^{(s)} = f_{rfl}^{(s)}P_{ir}^{(s)}$, $P_{rr}^{(p)} = f_{rfl}^{(p)}P_{ir}^{(p)}$, of the reflected power, ascribed to the reflected GO ray *rr*. The *rr* ray emerges from point O at an angle $\pi - \theta_0$ with respect to the evanescent ray *er* and is further traced according to the GO laws (3), (5). The remaining power fractions $(1 - f_{rfl}^{(s)})P_{ir}^{(s)}$, $(1 - f_{rfl}^{(p)})P_{ir}^{(p)}$ propagate along the evanescent ray *er* into the overdense plasma, and are distributed among the mesh zones $j = 1, 2, \ldots, N$, crossed by the *er* ray, in proportion to the rescaled absorption fractions $\tilde{f}_{aj}^{(s)}$, $\tilde{f}_{aj}^{(p)}$ as described in Section 2.4 below. For brevity, the upper polarization indices (s) and (p) are omitted in all the formulae below.

2.2. Solution in the wave-optics zone

Let z be the coordinate along the evanescent ray *er*, starting with $z = z_0$ at point O, and ending with $z = z_N$ upon exit from the simulation domain. Propagation of the *s*-polarized monocromatic wave across an inhomogeneous planar layer $z_0 \le z \le z_N$ is described by the Helmholtz equation [14, §88]

$$\frac{d^2E}{d\bar{z}^2} + (\varepsilon - \varepsilon_0 \sin^2\theta_0)E = 0, \quad H = -i\frac{dE}{d\bar{z}}, \tag{6}$$

for the complex amplitude E of the electric field, perpendicular to the plane of incidence; H is the magnetic field in the plane of incidence, and $\bar{z} = z\omega/c$. For the *p*-polarization, the corresponding wave equation is

$$\frac{d}{d\bar{z}}\left(\frac{1}{\varepsilon}\frac{dH}{d\bar{z}}\right) + \left(1 - \frac{\varepsilon_0 \sin^2\theta_0}{\varepsilon}\right)H = 0, \quad E = \frac{i}{\varepsilon}\frac{dH}{d\bar{z}}, \tag{7}$$

where E lies in the plane of incidence, and H is perpendicular to it. At interfaces where $\varepsilon(z)$ is discontinuous, the field amplitudes E and H must be continuous. The boundary conditions are set by assuming that the electromagnetic field at $z < z_0$ is a superposition of an incident (at an angle θ_0 with respect to the z-axis) and a reflected wave, while at $z > z_N$ only a transmitted wave is present. A consistent problem formulation requires

that the dielectric permittivity ε_0 at $z < z_0$ be real and positive, while the permittivity ε_∞ at $z > z_N$ must only be real.

Having found the consecutive intersections $\bar{z}_j$ of the evanescent ray *er* with the cell faces of the main 2D (3D) grid, one obtains a 1D partition of the full segment $[\bar{z}_0, \bar{z}_N]$ into N intervals $[\bar{z}_{j-1}, \bar{z}_j]$, $j = 1, \ldots, N$, with $\varepsilon(\bar{z})$ being given by a piecewise constant function

$$\varepsilon(\bar{z}) = \varepsilon_j, \quad \bar{z} \in [\bar{z}_{j-1}, \bar{z}_j], \tag{8}$$

where every ε_j is computed from the known material parameters in the corresponding 2D (3D) cell. Then, the piecewise analytical solution of Eqs. (6) and (7) can be written as

$$\left.\begin{array}{ll} s\text{-wave:} & E_j \\ p\text{-wave:} & H_j \end{array}\right\} = A_j^+ e^{i\kappa_j(\bar{z}-\bar{z}_{j-1})} + A_j^- e^{-i\kappa_j(\bar{z}-\bar{z}_{j-1})}, \tag{9}$$

where

$$\kappa_j \equiv \kappa_j' + i\kappa_j'' = \sqrt{\varepsilon_j - \varepsilon_0 \sin^2\theta_0^2}, \tag{10}$$

and $A_j^\pm$ are integration constants to be determined from the boundary conditions. This solution represents a typical realization of the finite analytic method [6, 7] for the 1D Helmholtz wave equation. Expressions for the complimentary field components (H_j for the *s*-wave, E_j for the *p*-wave) are obtained by differentiating (9) with respect to $\bar{z}$ as prescribed by Eqs. (6) and (7). To include the boundary conditions at $\bar{z} = \bar{z}_0 - 0$ and $\bar{z} = \bar{z}_N + 0$ into the general scheme, it is convenient to extend the variation of index j from $j = 1, \ldots, N$ to $j = 0, 1, \ldots, N+1$ by assuming $\bar{z}_{-1} = \bar{z}_0 - 0$ and $\varepsilon_{N+1} = \varepsilon_\infty$ in the above equations.

Because Eqs. (6) and (7) are linear, one can initially choose an arbitrary normalization for the field amplitudes $A_j^\pm$, and afterwards rescale the obtained solution to match the incoming GO power flux at point *O*. Having introduced a 2-vector

$$\mathbb{A}_j = \left\| \begin{array}{c} A_j^+ \\ A_j^- \end{array} \right\|, \quad j = 0, 1, \ldots, N+1, \tag{11}$$

we adopt the boundary conditions at $\bar{z} = \bar{z}_0 - 0$ and $\bar{z} = \bar{z}_N + 0$ in the form

$$\mathbb{A}_0 = \left\| \begin{array}{c} 1 \\ r \end{array} \right\|, \quad \mathbb{A}_{N+1} = \left\| \begin{array}{c} p \\ 0 \end{array} \right\|, \tag{12}$$

corresponding to a unity amplitude $A_0^+ = 1$ of the incident wave; accordingly, r and p are unknown complex amplitudes of the reflected and transmitted waves. Having demanded the E, H field components to be continuous at $\bar{z} = \bar{z}_j$, we obtain the linear recurrent relations

$$\mathbb{A}_{j+1} = \mathbb{G}_j \mathbb{A}_j = \mathbb{H}_j \mathbb{A}_0, \quad j = 0, 1, \ldots, N, \tag{13}$$

where

$$\mathbb{H}_j = \mathbb{G}_j \cdot \mathbb{G}_{j-1} \cdot \ldots \cdot \mathbb{G}_0, \tag{14}$$

$$\mathbb{G}_j = \left\| \begin{array}{cc} \frac{1}{2}(1+\gamma_j)e^{\Delta_j} & \frac{1}{2}(1-\gamma_j)e^{-\Delta_j} \\ \frac{1}{2}(1-\gamma_j)e^{\Delta_j} & \frac{1}{2}(1+\gamma_j)e^{-\Delta_j} \end{array} \right\|, \tag{15}$$

$$\Delta_j = i\kappa_j \Delta\bar{z}_j \equiv i\kappa_j(\bar{z}_j - \bar{z}_{j-1}), \tag{16}$$

$$\gamma_j = \left\{ \begin{array}{ll} \kappa_j/\kappa_{j+1}, & s\text{-wave}, \\ (\kappa_j\varepsilon_{j+1})/(\kappa_{j+1}\varepsilon_j), & p\text{-wave}. \end{array} \right. \tag{17}$$

Note that $\det \mathbb{G}_j = \gamma_j$.

Having computed the matrix $\mathbb{H}_N$, one readily finds the two unknown amplitudes r and p from the two linear equations

$$\left\| \begin{array}{c} p \\ 0 \end{array} \right\| = \mathbb{H}_N \left\| \begin{array}{c} 1 \\ r \end{array} \right\|, \tag{18}$$

which yield

$$r = -H_{N,21}\, H_{N,22}^{-1}, \quad p = -\left(\prod_{j=0}^{N} \gamma_j\right) H_{N,22}^{-1}; \tag{19}$$

here $H_{N,jk}$ is the jk-th element of matrix $\mathbb{H}_N$. Once the reflection amplitude r is known, all the field amplitudes $A_j^\pm$ are calculated from the recurrent relations (13). Because successive multiplication of many $\mathbb{G}_j$ matrices with large exponential terms may easily cause arithmetic overflow, practical implementation of the above algorithm requires additional technical rescaling described in the Appendix.

The flow and dissipation of laser energy along the *er* ray is represented by the z-component of the Poynting vector

$$S_z(\bar{z}) = \pm\frac{c}{8\pi}\Re(EH^*), \tag{20}$$

where H^* is the complex conjugate of H, and the $+/-$ sign corresponds, respectively, to the *s*- and *p*-polarizations. In view of an a priori arbitrary normalization of E (or H), it is convenient to introduce a uniquely defined dimensionless Poynting vector

$$\bar{S}_z(\bar{z}) = S_z(\bar{z})/S_{z0}^+, \tag{21}$$

normalized to the unit incident flux; here S_{z0}^+ is the z-component of the energy flux in the incident wave at $\bar{z} = \bar{z}_0$. For the boundary condition (12) we have

$$S_{z0}^+ = \frac{c}{8\pi}\left\{ \begin{array}{ll} n_0 \cos\theta_0, & s\text{-wave}, \\ n_0^{-1}\cos\theta_0, & p\text{-wave} \end{array} \right., \tag{22}$$

where $n_0 = \sqrt{\varepsilon_0}$. Clearly, $\bar{S}_z(\bar{z})$ is invariant with respect to rescaling of the field amplitudes $A_j^\pm$.

Finally, the reflected, f_{rfl}, and the transmitted, f_{tr}, fractions of the incident energy flux are given by

$$f_{rfl} \equiv 1 - \bar{S}_z(\bar{z}_0) = |r|^2, \quad (23)$$

$$f_{tr} \equiv \bar{S}_z(\bar{z}_N + 0) = \beta'_{N+1}\,|p|^2. \quad (24)$$

The fraction f_{aj}, absorbed within the interval $[\bar{z}_{j-1}, \bar{z}_j]$ along the *er* ray, is calculated as

$$f_{aj} \equiv \bar{S}_z(\bar{z}_{j-1}) - \bar{S}_z(\bar{z}_j) = f_{aj,sec} + f_{aj,osc}, \quad (25)$$

$$f_{aj,sec} = \beta'_j \left[\left|A_j^+\right|^2 \left(1 - e^{-2\kappa''_j \Delta\bar{z}_j}\right) + \left|A_j^-\right|^2 \left(e^{2\kappa''_j \Delta\bar{z}_j} - 1\right) \right], \quad (26)$$

$$f_{aj,osc} = 2\beta''_j\, \Im\left[A_j^+ A_j^{-*} \left(e^{2i\kappa'_j \Delta\bar{z}_j} - 1\right)\right], \quad (27)$$

where

$$\beta_j \equiv \beta'_j + i\beta''_j = \begin{cases} \kappa_j/\kappa_0, & s\text{-wave}, \\ (\kappa_j\varepsilon_0)/(\kappa_0\varepsilon_j), & p\text{-wave}. \end{cases} \quad (28)$$

The term $f_{aj,sec}$ is of secular nature: it is everywhere non-negative and corresponds to monotonic (with the increasing $\Delta\bar{z}_j$) attenuation of the incident and reflected waves. The term $f_{aj,osc}$, on the contrary, is of oscillatory nature: it can be both positive and negative and represents interference between the incident and reflected waves. The law of energy conservation is expressed by the identity

$$f_{rfl} + f_{tr} + \sum_{j=1}^{N} f_{aj} = 1, \quad (29)$$

which holds separately for both polarizations and manifests full conservativeness of our finite analytic algorithm.

With thus introduced fractional coefficients, the power balance between the GO and WO solutions at the transition point *O* is established as follows: if P_{ir} is the power fraction of the incident GO ray *ir* in the chosen (*s*- or *p*-) polarization, then $f_{rfl}P_{ir}$ is the reflected power fraction with the same polarization which propagates along the reflected GO ray *rr*; $f_{aj}P_{ir}$ is the power fraction absorbed in cell *j* along the evanescent ray *er*, and $f_{tr}P_{ir}$ is the power fraction which escapes the computational region along the *er* ray.

2.3. Criterion for transition to the 1D wave optics

The necessary condition for applicability of the GO approximation to the above WO solution reads [14, §88]

$$\frac{c}{\omega}\left|\frac{d}{dz}\left(\varepsilon_{cp} - \varepsilon_0 \sin^2\theta_0\right)^{-1/2}\right| \ll 1. \quad (30)$$

Hence, recalling that the *z*-direction is along the $\nabla\bar{n}_e$ vector and setting $\varepsilon_0 = 1$ (to conform with the limit of $\bar{n}_e \ll 1$ in Eq. (4)), one concludes that the transition to the wave optics should be made whenever a location with

$$\lambda\left|\nabla(\cos^2\theta_0 - \bar{n}_e)^{-1/2}\right| \geq a \quad (31)$$

is reached, where $a > 0$ is a certain dimensionless parameter of order unity. After some algebra inequality (31) can be rewritten as

$$\bar{n}_e + \left(\frac{\lambda}{2a}\,|\nabla\bar{n}_e|\right)^{2/3} \geq \cos^2\theta_0. \quad (32)$$

The physical meaning of condition (32) in the GO domain is quite transparent: one has to switch over to WO when either (i) the singular point $\varepsilon_{cp} = \sin^2\theta_0$ of Eq. (7) is approached (for $|\theta_0| \ll 1$ it means approaching the critical surface), or (ii) the gradient $\nabla\bar{n}_e = -\nabla\varepsilon_{cp}$ becomes too steep. For practical applications, condition (32) can be somewhat simplified by omitting the power 2/3 in the second term (which weakens to a certain extent the impact of this term), and generalized by introducing an additional free parameter on its right-hand side. Finally, we adopt a transition criterion in the form

$$\bar{n}_e + \beta_{gw}\lambda\,|\nabla\bar{n}_e| \geq \alpha_{gw}\cos^2\theta_0, \quad (33)$$

where $0 < \alpha_{gw} < 1$ and $\beta_{gw} \simeq 1$ are user-defined free parameters. Numerical tests show that for most practical applications a reasonable choice would be $\beta_{gw} = 1$ and $\alpha_{gw} = 0.8$–0.9.

2.4. Rescaling of the WO deposition profile

By an attempt to literally implement the proposed hybrid model, one encounters the following difficulty: when making a transition from the GO to the WO treatment, the specific (per unit volume) laser heating power Q often experiences a jump at the transition point *O*, whose direction and magnitude appear to vary randomly with either a changing plasma configuration, or by insignificant variations of the threshold parameter α_{gw}. This discontinuity is caused by the interference between the incident and reflected waves in the WO solution, which gives rise to a quasi-periodic standing-wave profile of $Q(z)$ along the evanescent ray (see Fig. 7 below). Depending on the phase of the standing wave at the transition point *O*, the value of Q may jump either up or down from its GO value. Apparently, this predicament becomes particularly troublesome when the laser wavelength λ is comparable or larger than the mesh-cell size.

An obvious recipe to ensure a smooth match between the GO and WO deposition powers at the transition point would be to suppress the oscillating interference terms $f_{aj,osc}$ when calculating f_{aj} in Eq. (25) — because

in the limit of GO (i.e. in the limit of $\lambda \to 0$) these terms average to zero. If, however, one simply puts $f_{aj,osc} = 0$, the law of energy conservation (29), rewritten as

$$f_{rfl} + f_{tr} + f_{a,sec} + f_{a,osc} = 1, \tag{34}$$

where

$$f_{a,sec} \equiv \sum_{j=1}^{N} f_{aj,sec}, \quad f_{a,osc} \equiv \sum_{j=1}^{N} f_{aj,osc}, \tag{35}$$

becomes violated unless $f_{a,osc} = 0$. To restore rigorous energy conservation, we adopt the following rescaling procedure for the secular terms $f_{aj,sec}$ which, to all practical needs, solves the problem.

More specifically, we preserve the reflected fraction f_{rfl} exactly as given by the WO solution in Section 2.2, and modify the quantities f_{tr}, f_{aj} to new values $\tilde{f}_{tr}$, $\tilde{f}_{aj}$ by distinguishing two cases depending on the sign of $f_{a,osc}$.

1. *Case* $f_{a,osc} \le 0$. In this case the sum $f_{a,sec}$ of only the secular terms overestimates the total absorption along the evanescent ray. The energy balance can be restored by simply cutting off the tail of the absorption profile in the evanescence zone. Let $j = \tilde{N} \le N$ be the last mesh zone from the WO solution for which

$$\tilde{f}'_a \equiv \sum_{j=1}^{\tilde{N}-1} f_{aj,sec} \le 1 - f_{rfl}. \tag{36}$$

Then the new absorption and transmission fractions are defined as

$$\tilde{f}_{aj} = \begin{cases} f_{aj,sec}, & 1 \le j < \tilde{N}, \\ \min\left(f_{a\tilde{N},sec},\, 1 - f_{rfl} - \tilde{f}'_a\right), & j = \tilde{N}, \\ 0, & j > \tilde{N}, \end{cases} \tag{37}$$

$$\tilde{f}_{tr} = 1 - f_{rfl} - \sum_{j=1}^{\tilde{N}} \tilde{f}_{aj}. \tag{38}$$

One readily ascertains that $0 \le \tilde{f}_{tr} \le f_{tr}$.

2. *Case* $f_{a,osc} > 0$. Now the secular terms alone are not sufficient to account for all the absorption in the WO region, and one has to "borrow" from the oscillatory part. Accordingly, we augment the values $f_{aj,sec}$ in proportion to the non-negative part

$$\hat{f}_{aj,osc} \equiv \max\left(0,\ f_{aj,osc}\right) \tag{39}$$

of the oscillating component of the absorption profile by setting

$$\tilde{f}_{aj} = f_{aj,sec} + \alpha_{osc}\, \hat{f}_{aj,osc}, \tag{40}$$

where the normalization factor α_{osc} is given by

$$\alpha_{osc} = f_{a,osc} \left(\sum_{j=1}^{N} \hat{f}_{aj,osc} \right)^{-1}. \tag{41}$$

Evidently, $0 < \alpha_{osc} \le 1$. The transmission fraction in this case is left intact, $\tilde{f}_{tr} = f_{tr}$.

3. Implementation in the RALEF-2D code

The numerical tests and application examples of the proposed model were calculated with the 2D radiation-hydrodynamics code RALEF [15, 16], which has been extensively used to simulate various laser-plasma problems [17, 18, 19]. The ray-tracing routines, required for implementation of the GO and WO parts of the algorithm, were adapted to the specific multi-block structure of the RALEF numerical mesh, composed of arbitrarily shaped quadrilateral cells. In the axisymmetric case, where the 2D mesh is constructed in the *rz* plane, all the elementary laser rays are assumed to lie in this plane.

The trajectory $\mathbf{x}_r(\tau)$ of every GO ray (i.e. of rays *ir* and *rr* in Fig. 1) is piecewise parabolic from cell to cell, as implied by the assumption of $\nabla\overline{n}_e$ being constant inside each mesh cell [1]. Possible jumps of n_e at cell interfaces are ignored, i.e. Snell's law is never applied at the inner cell interfaces; only a possibility of Snell's refraction upon the entry into the computational domain is foreseen.

Condition (33) for transition to WO is checked for the next to-be-entered cell by every crossing of a cell interface when tracing a GO ray: if fulfilled, the origin *O* of the evanescent ray is placed at the crossing point on this interface. The straight trajectory of the evanescent ray *er* is traced until it either exits the mesh, or the ray power P_r drops to an insignificant level (typically below 10^{-8} of its entrance value). The corresponding ordinary differential equations along the GO and WO segments of the traced rays are solved by the finite analytic method, i.e. piecewise analytically, assuming constant dielectric permittivity across every traversed cell.

A non-trivial issue for non-rectangular meshes is evaluation of the gradient ∇n_e. In RALEF all the principal variables, including the free-electron density n_e, are ascribed to cell centers. Evaluation of cell-centered values of ∇n_e is done in two steps on a 9-point stencil: (i) first, intermediate node values $n_{v,e}$ of n_e are calculated at all mesh nodes; this is done by a bilinear mapping of the auxiliary *c*-quadrilateral, composed of four cell centers surrounding a given vertex, onto a standard square $(\xi, \eta) \in [-1, +1] \times [-1, +1]$ [20, §11.4], followed

by a bilinear interpolation in the ξ, η-coordinates to the position of the given vertex on the standard square (a similar procedure is used in RALEF to evaluate the vertex values of temperature in the thermal-conduction algorithm [15]); (ii) second, a cell-local linear approximation $n_e(\mathbf{x}) = n_{c,e} + \mathbf{x} \cdot \nabla n_e$ is constructed within each mesh cell by minimizing the sum of squared deviations from the corresponding four node values $n_{v,e}$.

The described algorithm for calculating laser absorption is easily parallelized because the initial GO rays, entering the mesh, can be all treated independently. Therefore, when a simulation is carried out in the parallel mode on several tens of processors, RALEF can easily afford 30–100 rays per cell upon grid entry.

4. Numerical tests against exact 1D solutions

In the first place, the proposed hybrid model was tested against exact 1D solutions for a planar wave, incident from vacuum at a certain angle θ_0 on a 3-layer plane-parallel region $-\lambda \le z \le 2L + \lambda$ with a piecewise linear profile of the complex dielectric permittivity (see Fig. 2)

$$\varepsilon(z) = \begin{cases} \varepsilon_1, & -\lambda < z < 0, \\ \varepsilon_1 + \dfrac{z}{2L}(\varepsilon_{21} - \varepsilon_1), & 0 < z < 2L, \\ \varepsilon_3, & 2L < z < 2L + \lambda, \end{cases} \tag{42}$$

where λ is the laser wavelength. The first layer $-\lambda < z < 0$ with $\varepsilon_1 = 1$ represents vacuum and is added for the visualization purpose only. The end value

$$\varepsilon_{21} = -1 + i\varepsilon''_{21} \tag{43}$$

of the linear segment $0 < z < 2L$ is chosen such that the critical point, where $\Re(\varepsilon) = 0$, lies at a distance L from the vacuum boundary $z = 0$. Correspondence with the equivalent free-electron density, required for the GO part of the model, is established by assuming $\overline{n}_e = 1 - \Re(\varepsilon)$. The imaginary part $\varepsilon''_{21} > 0$ is typically small compared to 1 and adjusted such as to keep the reflected fraction f_{rfl} at normal incidence not far from 0.5. The third layer $2L < z < 2L + \lambda$ imitates a metallic film with an essentially zero transmission; in all the simulations its permittivity was set equal to

$$\varepsilon_3 = (4.0 + 8.4i)^2 = -54.56 + 67.2i, \tag{44}$$

which approximately corresponds to the permittivity of liquid tin at $\lambda = 1\ \mu$m [21].

Thus defined 1D problem was simulated with the 2D RALEF code in a rectangular region of the yz plane (the plane of incidence) as is shown in Fig. 3. The incident wave was represented by a GO beam with a transverse size of 0.4λ, split into 10^4 elementary rays. Two types of the 2D mesh were considered: (i) a simple square (or rectangular) mesh conforming to the isocontours of $\varepsilon(z)$, and (ii) a randomized mesh, where the nodes of the square mesh were randomly displaced by 20% from their original positions. The mesh resolution is characterized by the number n_L of intervals per distance L between the vacuum and the critical surface. All the test runs were done with the value $\beta_{gw} = 1$ in the transition criterion (33); if not stated to the contrary, the value $\alpha_{gw} = 0.8$ was used.

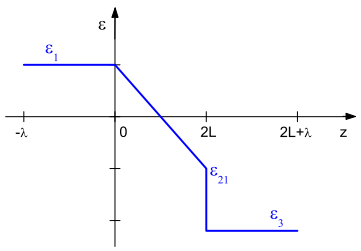

Figure 2: Profile of the dielectric permittivity [shown is only the real part $\varepsilon'(z)$] across a 3-layer slab used in 1D tests.

The RALEF results for the hybrid model are compared with those from the exact WO solutions. The exact WO solution for the s-polarized wave is expressed in terms of the Airy functions [22], which can be evaluated by using a highly accurate algorithm from Ref. [23]. For the p-polarization, a separate independent routine, based on the algorithm of Section 2.2, was written to obtain the WO solution with the required accuracy. As a simple figure of merit for assessing the accuracy of the hybrid model, the value of the absorption fraction $f_a = 1 - f_{rfl}$ by the considered 3-layer slab is used, namely, the relative error δ_a is defined as

$$\delta_a = \left| \frac{f_{a,n_L}}{f_a} - 1 \right|, \tag{45}$$

where f_{a,n_L} and f_a are the absorption fractions obtained, respectively, from a RALEF run with n_L mesh zones per L, and from the exact WO solution.

4.1. Absorption fraction

When the gradient of ε at $0 < z < 2L$ is so steep that $L \le \lambda$ and $\lambda|\nabla\overline{n}_e| \ge 1$, the condition (33) is fulfilled everywhere in the non-vacuum region $z > 0$. The latter means that every elementary GO ray should switch to the WO mode immediately upon entering the"plasma" zone $z > 0$. Hence, one would expect both the reflected,

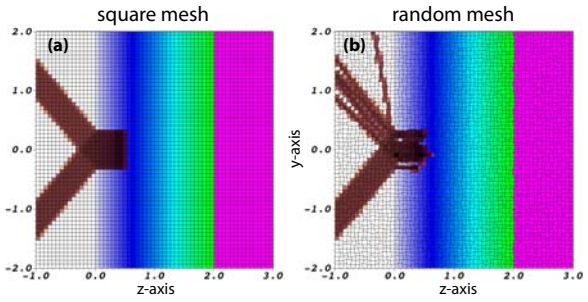

Figure 3: (Color online) 2D simulation of reflection of a laser beam (brown) from a half-space with a linearly ramped ε profile (42) for $L = \lambda$, $\theta_0 = 50°$, $n_L = 15$ and two types of numerical mesh. All the distances are measured in units of λ. The color palette at $z > 0$ illustrates variation of ε along the z-axis.

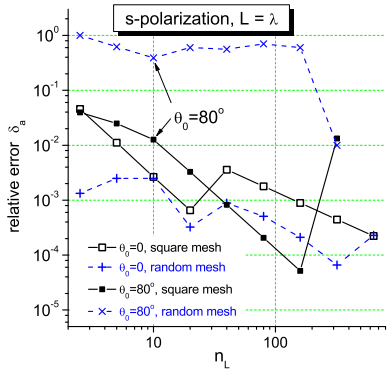

Figure 4: Relative error δ_a in the absorbed fraction f_a of the s-wave in the case of $L = \lambda$ ($\varepsilon''_{21} = 0.1$) as a function of n_L for two values of the angle of incidence $\theta_0 = 0$ and $\theta_0 = 80°$.

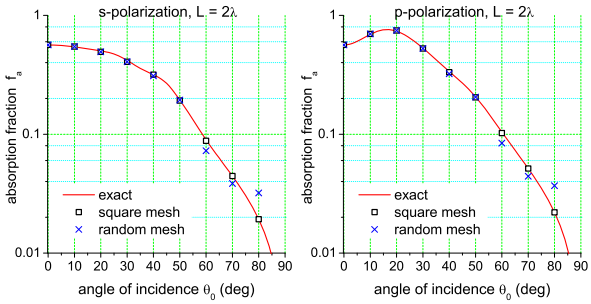

Figure 5: Absorption fraction f_a of the s-polarization (left) and p-polarization (right) on the ε profile (42) as a function of the incidence angle θ_0 for $L = 2\lambda$, $\varepsilon''_{21} = 0.05$ and $n_L = 40$.

f_{rfl,n_L}, and the absorbed, $f_{a,n_L} = 1 - f_{rfl,n_L}$, energy fractions to converge to the exact WO values as $n_L \to \infty$. As shown in Fig. 4, this is indeed the case for the square mesh, but not for the random mesh.

The finite analytic algorithm of Section 2.2 has the second convergence order ($\delta_a \propto n_L^{-2}$) to the exact WO solution, which is neatly reproduced by both square-mesh curves in Fig. 4 for not too high values of n_L. A kink, observed on either of these curves above a certain threshold value of n_L and followed by transition to the first convergence order, is explained by finite errors in numerical evaluation of $\nabla\bar{n}_e$. While the discontinuity of $\nabla\bar{n}_e$ at $z = 0$ is treated exactly in the finite-analytic solver, it is smeared over two monolayers of grid cells, adjacent to the $z = 0$ boundary, within the general RALEF algorithm for evaluation of gradients. Therefore, for sufficiently large n_L (for $n_L > 20$ at $\theta_0 = 0$), inequality (33) ceases to be fulfilled in the first cell at $z > 0$, which is then treated in the GO approximation and introduces a finite relative error to the deposition rate within that cell.

Unlike for the square mesh — where the direction of $\nabla\bar{n}_e$ is reproduced exactly and only its magnitude has a finite error in the first cell at $z > 0$ — on a random mesh also the direction of $\nabla\bar{n}_e$ has a finite (i.e. not vanishing for $n_L \to \infty$) scatter in all mesh cells. As a consequence, we see a pronounced scatter in the direction of the reflected beam in Fig. 3b. Therefore, no convergence for δ_a can be expected in this case: as n_L increases, the error δ_a in Fig. 4, calculated for the random mesh, fluctuates near a level which stays comfortably below 1% for $\theta_0 = 0$ but approaches 50–100% for $\theta_0 \gtrsim 80°$. To restore general convergence, one would have to implement a more accurate (i.e. converging to the exact result as $n_L \to \infty$) algorithm for evaluation of $\nabla\bar{n}_e$ on an arbitrary quadrilateral grid — not a trivial and practically hardly warranted task. Clearly, such a higher-order scheme for $\nabla\bar{n}_e$ must eliminate the angular scatter of the reflected light, observed in Fig. 3b, as $n_L \to \infty$.

For more shallow gradients of n_e, where the term $\beta_{gw}\lambda|\nabla\bar{n}_e|$ becomes noticeably less than 1, the convergence of the hybrid model to the exact WO results is lost even for the square mesh because now a finite portion of the $\varepsilon(z)$ ramp is treated in the GO approximation. The accuracy of our model for such cases is illustrated in Figs. 5 and 6, where the RALEF results for $f_a(\theta_0)$ are compared, respectively, with the exact WO values for the cases of $L = 2\lambda$ ($\varepsilon''_{21} = 0.05$) and $L = 10\lambda$ ($\varepsilon''_{21} = 0.01$); in both cases the number of cells per L was fixed at $n_L = 40$. It is seen that on the square mesh the exact WO values of f_a are reproduced quite accurately (with a typical error not exceeding 1–3%) for both polarizations and at all angles of incidence. Poor accuracy is only observed on random meshes at large angles of incidence onto steep gradients with $L \sim \lambda$. As already mentioned, to improve the accuracy in such cases, one would need a higher-order algorithm for evaluating $\nabla\bar{n}_e$

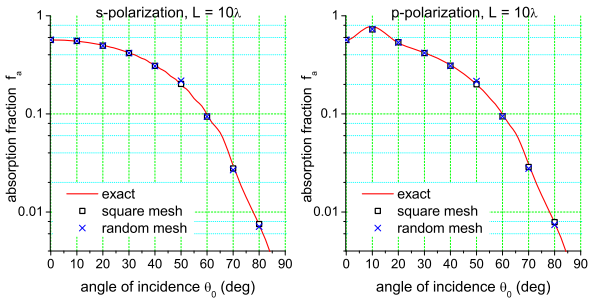

Figure 6: Same as Fig. 5 but for $L = 10\lambda$ and $\varepsilon''_{21} = 0.01$.

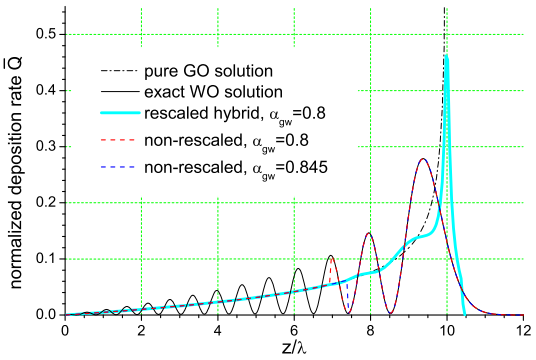

Figure 7: (Color online) Profiles of the normalized energy deposition rate $\bar{Q}(z)$ along an elementary ray normally incident upon the critical surface at $z = L = 10\lambda$ for the 1D test problem (42), (43). The oscillating thin black curve is the exact WO solution. The hybrid-model profile, shown with a thick cyan curve, consists of two segments: the GO segment at $z < 6.95\lambda$, and the rescaled WO segment at $z > 6.95\lambda$. The red and blue dashed curves show the hybrid-model profiles, calculated without the rescaling procedure of Section 2.4 for two different values of the transition parameter α_{gw}. The dash-dotted curve displays the pure GO solution.

on distorted quadrilateral grids.

4.2. Energy deposition profile

As described in Section 2.2, transition from the GO to the WO solution always preserves continuity of the energy flux, i.e. of the normal component $S_z(z)$ of the Poynting vector. This, however, is not the case for the volume-specific energy deposition rate

$$Q(z) = -\frac{dS_z}{dz}, \tag{46}$$

which can experience strong jumps at the transition point O. The latter is vividly illustrated in Fig. 7 with the profile of the normalized deposition rate

$$\bar{Q}(z) = -\frac{\lambda}{S_0}\frac{dS_z}{dz} \tag{47}$$

for a moderately shallow gradient of $\varepsilon(z)$ in Eq. (42) with $L = 10\lambda$, $\varepsilon''_{21} = 0.01$, where, at normal incidence, the exact WO profile exhibits 13 standing-wave maxima; S_0 in Eq. (47) is the incident energy flux at $z = 0$. The two dashed curves in Fig. 7 demonstrate what happens when the original (i.e. not rescaled as described in Section 2.4) WO deposition profile is simply attached to the GO profile at the transition point where the condition (33) is fulfilled: depending on the value of the free parameter α_{gw}, the GO deposition rate Q may either jump up by about a factor 2, or jump down by more than an order of magnitude. Clearly, such a behavior can hardly be tolerated in hydrodynamic simulations of laser plasmas.

In other words, our hybrid model, being eclectic in nature, in principle cannot lead to a smooth match between the GO and the rigorous WO energy deposition profiles. Therefore, looking for a practical solution, we choose to modify the rigorous WO profile by applying the rescaling (redistribution) procedure from Section 2.4 and put up with the incurred potentially significant distortion of this profile near the critical surface. At the same time (as it follows from the formulae of Section 2.4), we fully preserve the accuracy for the overall absorption fraction f_a, demonstrated in Section 4.1.

The corresponding rescaled $\bar{Q}(z)$ profile, calculated for $\alpha_{gw} = 0.8$, is plotted in Fig. 7 as the thick cyan curve: it smoothly matches the GO profile at $z = 6.95\lambda$ and undergoes hardly noticeable (typically within 1–3%) variations when the value of α_{gw} is changed. As might be expected, in the limit of $\lambda \ll L$ the rescaled hybrid $\bar{Q}(z)$ curve approaches the purely GO deposition profile — shown in Fig. 7 as a thin dash-dotted curve — everywhere except the immediate vicinity of the critical surface. It should be reminded that the pure GO profile of $\bar{Q}(z)$ diverges as z approaches the critical surface with $\varepsilon' = 0$, manifesting a weak integrable singularity that is difficult to resolve numerically (in our example, with 20 mesh cells per λ, the highest point on the GO plot of $\bar{Q}(z)$ in Fig. 7 is $\bar{Q} = 1.16$ at $z = 9.975\lambda$). The hybrid profile, on the contrary, always peaks at a finite value, which typically exceeds the corresponding WO maximum by about a factor 1.3–1.6. At the same time, the hybrid peak of $\bar{Q}(z)$ turns out to be noticeably narrower than the last WO peak because of the enforced spatial redistribution of the oscillating interference terms: its width is determined by the skin depth immediately behind the critical surface.

Note that in the opposite limit of steep gradients, $L \ll \lambda$, as the geometric optics becomes inapplicable, the rescaled hybrid profile of $\bar{Q}(z)$ approaches the exact WO curve; in the extreme case of a step-like vari-

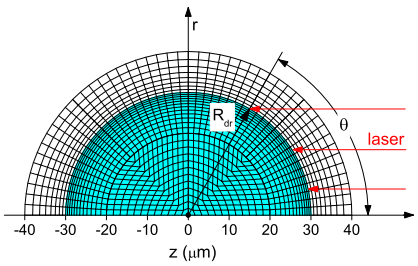

Figure 8: Schematic view of a spherical tin droplet of radius R_{dr} = 30 μm (shaded), projected onto the computational domain of radius 40 μm in the rz-plane. Depicted is a crude version of the numerical mesh used in the simulation.

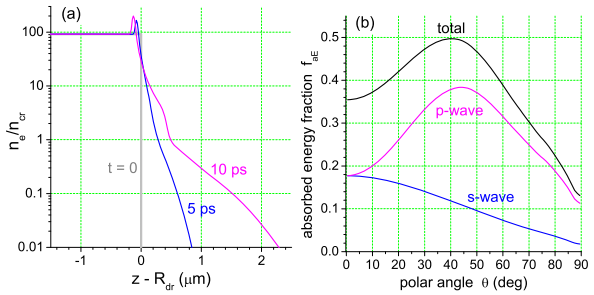

Figure 9: (a) Profiles of the dimensionless free-electron density $\bar{n}_e = n_e/n_{cr}$ along the z-axis (i.e. at $\theta = 0$) in the vicinity of the boundary with vacuum at three characteristic times during the 10-ps laser pulse. (b) Fraction of the incident laser energy, absorbed by the droplet within 10 ps, as a function of the local position on the droplet surface (where the corresponding elementary ray would hit the initial droplet surface), measured by its value of the polar angle θ. For the unpolarized incident beam, the total absorption fraction is the sum of contributions from the s- and p-waves.

ation of $\varepsilon(z)$ between vacuum and cold metal [$L = 0$ in Eq.(42)], it coincides with the exact WO solution because we have $A_j^- = 0$ at $z > 0$ and all the oscillating terms (27) vanish.

5. 2D application examples

5.1. Absorption of a 10-ps laser pulse by a spherical droplet of tin

In this example we consider a short 10-ps laser pulse incident on a spherical droplet of tin with a constant (in space and time) intensity of $I_{las} = 10^{13}$ W/cm^2; see Fig. 8. This problem is particularly relevant for applications to the extreme ultraviolet (EUV) lithography [24, 25, 26], where such pulses are considered as a promising option for preconditioning mass-limited tin targets to maximize the generation of the 13.5-nm EUV light. As in the experiments of Ref. [26], we set the radius of the droplet equal to $R_{dr} = 30$ μm. The problem is essentially 2D because the entire configuration is axially symmetric with respect to the laser-beam axis (the z-axis).

The simulations were done with the RALEF code in its full operation mode, where full account was taken of the hydrodynamic expansion, thermal conduction and radiative energy transport. The adaptive numerical mesh had a topological structure displayed in Fig. 8, with 360 zones over the π interval of the polar angle θ, and with 200 radial zones over the interval 20 μm $\leq r \leq$ 40 μm, i.e. with the total of 88200 mesh cells over the simulated half-circle in the rz plane. The mesh was progressively refined in radial direction to a resolution of 15 nm (comparable to, but not smaller than the skin depth) near the liquid-vacuum interface. The initial state of liquid tin was chosen at $\rho_0 = 6.05$ g/cc, $T_0 = 0.1$ eV, which corresponds to a practically zero pressure according to the employed equation of state. The outer layer 30 μm $\leq r \leq$ 40 μm was assumed to be filled with a tenuous tin vapor at a density $\rho_{v0} = 10^{-10}$ g/cc. For the laser pulse, box-like temporal and spatial profiles were used, with the total pulse duration $t_{las} = 10$ ps and the focal spot radius $r_{foc} = 31$ μm (exceeding by 1 μm the initial droplet radius R_{dr}). The beam was split into 5000 equidistant (along the r coordinate) elementary rays. The laser wavelength was set equal to $\lambda = 1$ μm, and the incident light was assumed to be unpolarized.

By $t = 10$ ps the ablated tin plasma is heated to a maximum temperature of $T \approx 200$ eV and expands by about 4 μm (see Fig. 9a). Radiative energy losses are not significant and amount to $\approx 5\%$ of the absorbed laser energy. To calculate the dielectric permittivity, given by Eq. (2), over the entire range of states from a liquid metal to a hot plasma, a semi-empirical model for the electron-ion collision frequency ν_{ei} from Ref. [3] was used. This model contains a single free parameter, used to fit the known reflectivity of tin [21] near the normal conditions.

The $\bar{n}_e$ profiles in Fig. 9a confirm that the effect of hydrodynamic expansion cannot be neglected when calculating the absorption of a 10-ps pulse because it smears the sharp metal-vacuum boundary over a scale of ~ 1 μm, comparable to the laser wavelength λ. The physical situation is close to the case of $L = \lambda$ in the test problem of Section 4.1, where our model demonstrated good accuracy. The calculated profiles of the absorbed energy fraction f_{aE} along the irradiated surface of the droplet are plotted in Fig. 9b as a function of the polar angle θ for two polarization modes. A pronounced difference between the absorption of the s- and p-polarized components (assumed to be present in equal proportion in the incident light) has a strong impact on the distri-

bution of the total absorbed energy: because the total absorbed fraction $f_{aE}(\theta)$ peaks at $\theta \approx 40°$, the hottest spot on the irradiated droplet surface turns out to be not at its pole $\theta = 0$ but rather takes a form of an annulus at $\theta \simeq 35°$, where the product $f_{aE}(\theta)\cos\theta$ is maximum.

Although the present numerical example was not aimed at a detailed comparison with any particular experiment, it is worth mentioning that the measured absorption (see, for example, Ref. [27]) of short laser pulses exhibits similar values and behavior as that shown in Fig. 9b. This example demonstrates also that our model may serve as a practical and adequate option for theoretical modeling in two and three dimensions of a broad range of experiments with short laser pulses, where the diffraction of laser light is not important.

5.2. Ablation of a planar tin target by a CO_2 laser pulse

Our second example — also suggested by applications to the EUV lithography [24] — deals with an ablation of a planar tin layer by a relatively long (multi-nanosecond) pulse of a CO_2 laser, which has a relatively long wavelength of $\lambda = 10.6$ μm. Again, assuming an axi-symmetric laser beam, we have a 2D problem in the rz-plane. For the volume, which later becomes occupied by the ablated plasma, we used the same type of a quasi-spherical mesh as in the previous example, but within a single quadrant $z > 0$; see Fig. 10. At the outer boundary with a spherical radius of 250 μm, the condition of free outflow was imposed. A 2-μm thick layer of liquid tin was attached to the "vacuum" hemisphere at $z = 0$, with the boundary condition of a rigid reflecting wall at $z = -2$ μm. The initial state of the tin liquid and vapor was the same as in the previous case. The mesh size was 0.05×0.4 μm in the liquid foil, and 0.5×0.5 μm in the ablated plasma near the critical surface (i.e. at $z \simeq 30$–50 μm), where the laser was most effectively absorbed; the total number of mesh cells was 66200. A Gaussian spatial profile was chosen with the beam waist (i.e. full width at the e^{-2} level) of 50 μm; the beam was split into 2×10^4 elementary rays, equally spaced over the radial aperture of $0 < r < 50$ μm. The peak intensity on the axis was kept constant at $I_{las} = 7 \times 10^9$ W/cm^2.

With the laser intensity fixed in time, the 2D flow of the ablated tin plasma would be expected to reach a steady state after a certain relaxation time, which in our case is about 5 ns (see Fig. 11). By this time the critical surface at $n_e = n_{cr} = 10^{19}$ cm^{-3} pulls back from the liquid surface by a distance, comparable to the radius of the laser beam (some 30 μm in our case; see Fig. 12), and should, in principle, stabilize there. However, it is easy to ascertain that refraction in the GO zone above

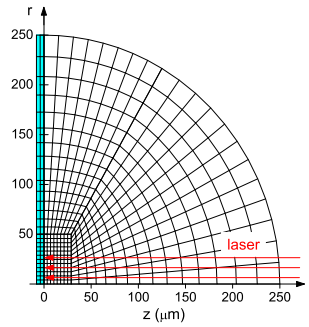

Figure 10: Schematic view of a planar foil of tin (at $z < 0$, shaded), projected onto the computational domain of radius 250 μm in the rz-plane. Depicted is a crude version of the numerical mesh used in the simulation.

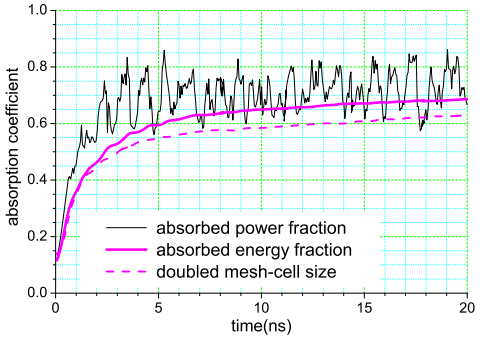

Figure 11: (Color online) Thin black curve: instantaneous absorption coefficient $f_{aP}(t)$, defined as the ratio between the absorbed and the incident laser powers. Thick solid magenta curve: time-integrated absorption coefficient $f_{aE}(t)$, defined as the ratio between the absorbed and the incident laser energies. Dashed magenta curve: time-integrated coefficient $f_{aE}(t)$, calculated on a grid with doubled mesh-cell dimensions along each direction.

the critical surface makes the plasma outflow unstable. Indeed, once a depression is formed in the n_e distribution (as is displayed by the $n_e = 10^{18}$ cm^{-3} isocontour near the beam axis in Fig. 12a), the laser light tends to be focused towards the bottom of such a depression and make it deeper (a hydrodynamic self-focusing instability [10]). Consequently, the density field and the position of the critical surface — as well as other physical quantities in the laser absorption zone — fluctuate in space and time, as is demonstrated by the $f_{aP}(t)$ plot in Fig. 11 and by the n_e isocontours in Figs. 12a and 12b.

Although the self-focusing instability of the RT model has a clear physical origin, its spatial and temporal scales are not expected to be correctly reproduced when the mesh cells become significantly smaller than the laser wavelength λ because of the absence of diffraction. This principal defect of the RT approach is, of course, fully carried over to the hybrid model, and the

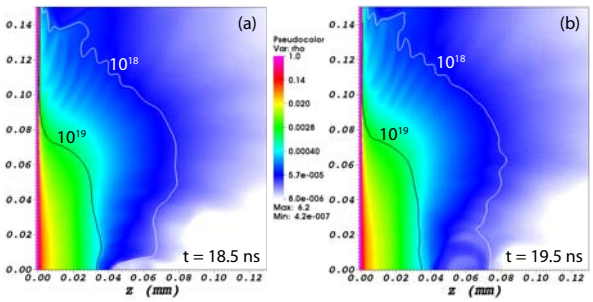

Figure 12: (Color online) 2D density distribution (in g/cc) of the ablated plasma plume in the rz-plane at two close time moments (a) t = 18.5 ns and (b) t = 19.5 ns. Shown also are two isocontours of the free electron density $n_e = 10^{18}$ cm^{-3} and $n_e = n_{cr} = 10^{19}$ cm^{-3}.

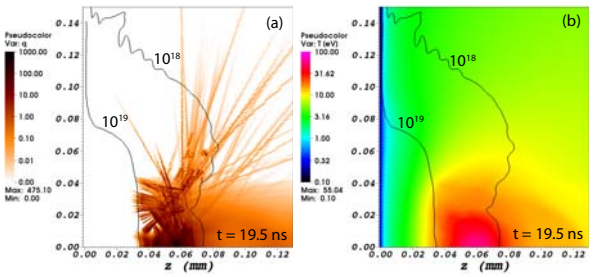

Figure 13: (Color online) 2D distribution (a) of the mass-specific rate q of the laser heating (in TW/mg), and (b) of the plasma temperature T (in eV) in the computational rz-plane at t = 19.5 ns. Shown also are the isocontours $n_e = 10^{18}$ cm^{-3} and $n_e = n_{cr} = 10^{19}$ cm^{-3}.

purpose of the present numerical example, where the ratio of λ to the relevant mesh-cell size is about 20, was to illustrate how the present model behaves in such situations.

Because the laser wavelength λ does not participate in the transport model, the minimum scale l_{vs} of the self-focusing instability is determined, on the one hand, by the mesh resolution, and, on the other hand, by physical stabilization mechanisms such as thermal conductivity and radiative energy transport. Without diffraction, the mass-specific laser deposition rate q, shown in Fig. 13a (in units of TW/mg), fluctuates on a spatial scale as small as the mesh-cell size. These fluctuations are, however, damped by thermal conduction and radiative transport, with the 2D temperature distribution in Fig. 13b looking rather smooth. Note that the radiative losses in this case are significant and amount to 37% of the absorbed laser energy. Comparison of Figs. 12a and 12b reveals that the plasma density in the corona region, where $n_e < n_{cr}$, experiences strong variations on a spatial scale down to $l_{vs} \simeq 5$ μm. The characteristic time scale of unstable behavior is then $t_{vs} \simeq l_{vs}/u \simeq 0.5$ ns, where $u \simeq 10^6$ cm/s is the characteristic hydrodynamic velocity. Accordingly, the instantaneous absorption coefficient $f_{aP}(t)$ in Fig. 11 exhibits irregular oscillations on this timescale.

The irregular laser reflection pattern, observed in Fig. 13a, is caused by a combination of two factors that are difficult to separate, namely, (i) by ripples on isocontours of n_e at $n_e < n_{cr}$ (physical instability), and (ii) by a relatively crude algorithm for calculating $\nabla\bar{n}_e$ (pure numerics). Because the transition criterion (33) is rather sensitive to both the magnitude and the direction of the gradient $\nabla\bar{n}_e$, the transition points O are widely scattered across an extended region with $0.1n_{cr} \lesssim n_e < n_{cr}$. Consequently, we observe a wide scatter in the directions of both the evanescent and reflected rays. And even if a more accurate scheme were implemented for $\nabla\bar{n}_e$, a strongly rippled shape of n_e isocontours suggests that, unlike in Fig. 3, one could hardly expect the laser reflection from the critical surface to become noticeably more regular than in Fig. 13a.

Having accepted that both the amplitude and the timescale of unstable variations of the absorbed laser power cannot be adequately reproduced by the RT and hybrid models, we do, in fact, lose confidence in the time-integrated absorption coefficient $f_{aE}(t)$ as well — despite the fact that its temporal behavior is rather smooth. And though the calculated values of f_{aE} appear reasonable from the physics point of view and from what is known from the experiments, this is the issue which cannot be resolved without detailed comparison with a more accurate model that fully includes the diffraction effects.

As a practical recommendation, it can be advised to avoid doing multidimensional simulations of long laser pulses with the present hybrid model on numerical grids, where the mesh-cell size in the absorption zone is considerably smaller than the laser wavelength. To give a feeling for possible influence of the mesh resolution, the dashed curve in Fig. 11 shows the time-integrated absorption coefficient $f_{aE}(t)$, calculated on a two times cruder mesh with 1×1 μm mesh cells in the laser absorption zone; the corresponding plot of $f_{aP}(t)$ (not shown in Fig. 11) exhibits irregular variations with practically the same amplitude and on the same time scale as the base case. One can also introduce artificial stabilization by setting a certain lower limit $\bar{n}_e \geq \bar{n}_{gw0} \simeq 0.03$–$0.1$ on the free electron density before checking the transition criterion (33) (the results in Figs. 11–13 were calculated with $\bar{n}_{gw0} = 0.1$), augmented by a corresponding lower limit on the value of $\cos^2\theta_0$ in this criterion.

5.3. Computational efficiency of the hybrid model

Generally, the numerical cost of our hybrid model should not significantly exceed that of the pure RT method because for every incident elementary GO ray *ir* one has, in addition, to trace a single evanescent ray *er* in the WO zone, which might, on average, cross about one half of the 2D (3D) mesh. The numerical cost for the *er* ray to traverse a single mesh cell is roughly equivalent to computing several (about 4) exponentials. The latter means that if the laser beam has an aperture comparable to the transverse (with respect to the laser beam) size of the mesh, and if the number n_{rpc} of elementary rays per cell in the transverse direction is $n_{rpc} \simeq 1$, the numerical cost of laser deposition must be of the same order as the numerical cost of pure hydrodynamics. In the RALEF-2D code, executed in the sequential mode, the computational cost of laser deposition begins to exceed that of hydrodynamics (together with thermal conduction) for $n_{rpc} \gtrsim 3$. Note that the cost of 2D hydrodynamics (with the 2nd-order Godunov scheme, mesh adaptivity, and thermal conduction), being approximately 1 μs per 2D cell per hydrocycle, does not warrant its parallelization.

To reduce the numerical noise in the laser energy deposition due to a finite number of elementary rays, one would, of course, prefer to run simulations with $n_{rpc} > 10$–30. Because the numerical algorithm of the hybrid model is easily and effectively parallelized, the wall-clock CPU time, spent on laser transport in case of $n_{rpc} \gg 1$, can be kept on a par with the unparallelized hydrodynamics by running the code in a parallel mode: e.g. for $n_{rpc} \simeq 100$ some 30–40 processors would be sufficient.

The situation changes, however, when the 2D (3D) hydrodynamics is coupled to spectral radiation transport. As the computational cost of radiation transport by far exceeds that of hydrodynamics, the code is necessarily run in a parallel mode, and the CPU time, spent on the laser transport, generally becomes an insignificant fraction of the total computing time: in the RALEF-2D simulations with $n_{rpc} \simeq 100$ it typically lies below 10%. In the example of the previous section, simulated with $2{\times}10^4$ elementary rays ($n_{rpc} = 200$, which is already excessive), and with the S_{12} angular quadrature and 28 frequencies in radiation transport, the laser transport consumed about 15% of the total CPU time.

6. Conclusions

A hybrid model of laser deposition, combining the geometrical-optics ray tracing with the 1D solution of the Helmholtz wave equation, offers a relatively simple and computationally inexpensive way to extend the applicability of the traditional RT approach [1] to transition layers between the sub- and super-critical plasma regions, or between the vacuum and solid (liquid) metals. In this work a new improved version of such a model is proposed and investigated, which demonstrates good accuracy in description of the laser absorption on plasma density gradients at both normal and oblique incidence.

The hybrid model is particularly attractive for large-scale 2D and 3D hydrodynamic simulations, where the computing costs are often critical. One of its important advantages is the possibility to employ the finite analytic numerical method for calculating the penetration of laser light into supercritical evanescence zones, which yields physically adequate results even on relatively crude meshes relative to the skin depth. As a result, the present model can be successfully applied to a broad class of problems, where metal targets are irradiated by short pulses with not too high intensity so that the hydrodynamic self-focusing instability has no time to develop and various non-linear effects are not an issue.

At the same time, being essentially eclectic in nature, the hybrid model retains the main defect of the RT method, namely, a complete omission of diffraction. As a consequence, no convergence can be expected in a general 2D or 3D case to the exact wave-optics solution. Moreover, if the mesh cell size becomes too small compared to the laser wavelength and a sufficiently long pulse is applied, the development of the hydrodynamic self-focusing instability on unphysical spatial and temporal scales may significantly distort the overall pattern and intensity of the laser energy deposition in non-uniform plasmas.

Acknowledgments

This work was supported by the Russian Science Foundation through grant No. 14-11-00699.

Appendix A. Technical rescaling of the WO solution to avoid arithmetic overflow

To avoid arithmetic overflow by successive multiplication of $\mathbb{G}_j$ matrices in Eq. (14), one can factor out the growing exponents by introducing scaled matrices $\widetilde{\mathbb{G}}_j$ and $\widetilde{\mathbb{H}}_j$, defined as

$$\widetilde{\mathbb{G}}_j = e^{-\sigma_j}\mathbb{G}_j, \quad \widetilde{\mathbb{H}}_j = \widetilde{\mathbb{G}}_j \cdot \widetilde{\mathbb{G}}_{j-1} \cdot \ldots \cdot \widetilde{\mathbb{G}}_0 = e^{-\Sigma_j}\mathbb{H}_j, \tag{A.1}$$

where

$$\Sigma_j = \sigma_0 + \sigma_1 + \ldots + \sigma_j, \tag{A.2}$$

$$\sigma_j = \kappa_j'' \Delta\bar{z}_j \geq 0, \quad j = 0, 1, \ldots, N. \tag{A.3}$$

Then, the two unknown amplitudes r and p are calculated as

$$r = -\frac{\widetilde{H}_{N,21}}{\widetilde{H}_{N,22}}, \quad p = -\frac{e^{-\Sigma_N} \prod_{j=0}^{N} \gamma_j}{\widetilde{H}_{N,22}}, \tag{A.4}$$

where $\widetilde{H}_{N,jk}$ is the jk-th element of matrix $\widetilde{\mathbb{H}}_N$. As the value of Σ_N becomes very large compared to unity, Eq. (A.4) yields the correct final value of the reflection amplitude r, and a zero value of the transmission amplitude p.

References

[1] T. B. Kaiser, Phys. Rev. E 61 (2000) 895–905. doi:10.1103/PhysRevE.61.895.

[2] M. Born, E. Wolf, A. Bhatia, P. Clemmow, D. Gabor, A. Stokes, A. Taylor, P. Wayman, W. Wilcock, Principles of Optics: Electromagnetic Theory of Propagation, Interference and Diffraction of Light, Cambridge University Press, 1999.

[3] M. M. Basko, T. Löwer, V. N. Kondrashov, A. Kendl, R. Sigel, J. Meyer-ter Vehn, Phys. Rev. E 56 (1997) 1019–1031.

[4] M. E. Povarnitsyn, N. E. Andreev, P. R. Levashov, K. V. Khishchenko, O. N. Rosmej, Physics of Plasmas 19 (2012) 023110. doi:10.1063/1.3683687.

[5] N. Andreev, M. Povarnitsyn, M. Veysman, A. Faenov, P. Levashov, K. V. Khishchenko, T. Pikuz, A. Magunov, O. Rosmej, A. Blazevic, A. Pelka, G. Schaumann, M. Schollmeier, M. Roth, Laser and Particle Beams 33 (2015) 541–550. doi:10.1017/S0263034615000580.

[6] C.-J. Chen, H.-C. Chen, Journal of Computational Physics 53 (1984) 209 – 226. doi:10.1016/0021-9991(84)90038-X.

[7] C. Chen, M. Sheikholeslami, R. Bhiladvala, Computer Methods in Applied Mechanics and Engineering 75 (1989) 61 – 76. doi:10.1016/0045-7825(89)90015-7.

[8] Y. V. Afanas'ev, E. G. Gamalii, N. N. Demchenko, O. N. Krokhin, V. B. Rozanov, Sov. Phys. JETP 52 (1980) 425–431.

[9] I. P. Tsygvintsev, A. Y. Krukovskiy, V. A. Gasilov, V. G. Novikov, I. V. Popov, Mathematical Models and Computer Simulations 8 (2016) 382–390. doi:10.1134/S2070048216040153.

[10] A. Colaïtis, G. Duchateau, P. Nicolaï, V. Tikhonchuk, Phys. Rev. E 89 (2014) 033101. doi:10.1103/PhysRevE.89.033101.

[11] A. Colaïtis, G. Duchateau, X. Ribeyre, V. Tikhonchuk, Phys. Rev. E 91 (2015) 013102. doi:10.1103/PhysRevE.91.013102.

[12] W. Kruer, The physics of laser plasma interactions, Frontiers in physics, Addison-Wesley, 1988.

[13] Y. Kravtsov, Y. Orlov, Geometrical Optics of Inhomogeneous Media, Springer Series on Wave Phenomena, Springer Berlin Heidelberg, 2011.

[14] L. D. Landau, E. M. Lifshitz, Electrodynamics of Continuous Media, 2 ed., Pergamon Press, 1984.

[15] M. M. Basko, J. A. Maruhn, A. Tauschwitz, Journal of Computational Physics 228 (2009) 2175–2193. doi:10.1016/j.jcp.2008.11.031.

[16] M. M. Basko, J. A. Maruhn, A. Tauschwitz, Development of a 2D radiation-hydrodynamics code RALEF for laser plasma simulations, GSI Report 2010-1, PLASMA-PHYSICS-25, GSI Helmholtzzentrum für Schwerionenforschung GmbH, 2010.

[17] A. Tauschwitz, M. Basko, A. Frank, V. Novikov, A. Grushin, A. Blazevic, M. Roth, J. Maruhn, High Energy Density Physics 9 (2013) 158–166. doi:10.1016/j.hedp.2012.12.004.

[18] M. M. Basko, V. G. Novikov, A. S. Grushin, Physics of Plasmas 22 (2015) 053111. doi:10.1063/1.4921334.

[19] M. M. Basko, Physics of Plasmas 23 (2016) 083114. doi:10.1063/1.4960684.

[20] P. Wesseling, Principles of Computational Fluid Dynamics, Lecture Notes in Computer Science, Springer Berlin Heidelberg, 2001.

[21] G. Cisneros, J. S. Helman, C. N. J. Wagner, Phys. Rev. B 25 (1982) 4248–4251.

[22] V. Ginzburg, The propagation of electromagnetic waves in plasmas, International series of monographs on electromagnetic waves, Pergamon Press, 1970.

[23] A. Gil, J. Segura, N. M. Temme, Numerical Algorithms 30 (2002) 11–23. doi:10.1023/A:1015636825525.

[24] V. Bakshi, EUV Sources for Lithography, Press Monographs, SPIE Press, 2006.

[25] H. Mizoguchi, H. Nakarai, T. Abe, K. M. Nowak, Y. Kawasuji, H. Tanaka, Y. Watanabe, T. Hori, T. Kodama, Y. Shiraishi, T. Yanagida, G. Soumagne, T. Yamada, T. Yamazaki, S. Okazaki, T. Saitou, Proc. SPIE 9422 (2015) 94220C–94220C–13. doi:10.1117/12.2086347.

[26] A. Y. Vinokhodov, K. N. Koshelev, V. N. Krivtsun, M. S. Krivokorytov, Y. V. Sidelnikov, S. V. Medvedev, V. O. Kompanets, A. A. Melnikov, S. V. Chekalin, Quantum Electronics 46 (2016) 23–28. doi:10.1070/QE2016v046n01ABEH015867.

[27] D. Riley, L. A. Gizzi, A. J. Mackinnon, S. M. Viana, O. Willi, Phys. Rev. E 48 (1993) 4855–4858. doi:10.1103/PhysRevE.48.4855.